This is a peer-reviewed, accepted author manuscript of the following article: De Carvalho Faria Lima Lopes, B., & Tarantino, A. (Accepted/In press). Stability analysis of a cave excavated in granular cohesionless material. *Géotechnique*.

Stability analysis of a cave excavated in granular cohesionless material

Dr Bruna De Carvalho Faria Lima Lopes*
Department of Civil and Environmental Engineering, University of Strathclyde, G1 1XJ, Glasgow-UK
ORCID: 0000-0001-7669-7236
Prof Alessandro Tarantino
Department of Civil and Environmental Engineering, University of Strathclyde, G1 1XJ, Glasgow-UK
ORCID: 0000-0001-6690-748X

*** Corresponding author: bruna.lopes@strath.ac.uk**

Abstract

The paper presents the analysis of the long-term stability of a large unsupported cave excavated in granular cohesionless material in Ficulle, Italy. The stability of the cave arises from a 'cohesive' term in the shear strength criterion and this paper investigates the source of such cohesive term. Contrary to expectations, the material appeared to be granular (cohesionless) at the touch. The investigation started by determining whether the stability of the cave was owed to any cementation bonding the soil particles. Microstructural analyses, together with geomechanical testing produced enough evidence to suggest that the material is not naturally cemented. On the other hand, water-undrained direct shear tests on unsaturated intact specimens indicated the presence of significant apparent cohesion, which was then linked to the existence of suction in the material. In this way, the stability of the cave was assessed accounting for the beneficial effects of suction and partial saturation on shear strength. A 3-D analysis based on the upper bound theorem of plasticity was successful in confirming the stability of the cave for the state in which the structure was at the time of field investigation. In addition, it was shown that 24 and 48hrs rainfalls of 100 years return period are not sufficient to relieve suction enough to bring the cave to collapse, thus justifying the observed long-term stability of the cave. Suction is rarely included in geotechnical design under the assumption that it cannot be relied on due to the

potential adverse effect of rainwater infiltration. This case study demonstrates that suction can indeed naturally remain ‘active’ for long time contributing to the long-term stability of geo-structures.

Key words: granular cohesionless soil, cementation, suction, shear strength, cave, stability analysis

1. Introduction

Man-made caves and caverns have been excavated for a variety of applications for short and long-term access. Long lasting stability of centenary and millenary domestics and religious cavern structures in shallow rocks are found all over the planet. Examples of these structures are the underground tombs excavated by Egyptians in limestone (about 1,500 B.C.), Buddhist temples excavated in basalt lavas in several locations in India (from C2nd B.C. to C10th A.D.), underground cities in Cappadocia, Turkey, excavated in a Tertiary rhyolite ash-flow tuff (1st millennium A.D.), and underground villages in Tunisia, in which some have been continuously inhabited for 900 years (Knight 2003).

In contrast, examples of stability of man-made unsupported caves in soils are rare. In fact, a study reported by the Occupational Safety and Health Administration of the United States (OSHA) estimated that 100 people were killed in excavations cave-in each year (Thompson and Tanenbaun 1975), which eventually led the organisation to publish (1st edition published in 2001) an excavation standard (Peck and Halterman 2019) suggesting some requirements allowing for a stable excavation. Amongst the requirements is the ranking of soils and rocks deposits by order of stability. According to the standard, stable rock, cohesive and cemented material are on the top of the ranking while granular and granular cohesionless soils are at the bottom.

The reasoning for the poor performance of granular and granular cohesionless soils on the ranking list of the OSHA is that these materials have little or no cohesion effect, despite the fact that some partially saturated granular cohesionless soils exhibit apparent cohesion originated from their suction. Most standard authorities, practitioners and academicians still find it convenient to disregard the contribution of partial saturation to shear strength as this leads to conservative design (Stanier and Tarantino 2013).

In light of this, the case of an unsupported cave excavated in granular material is presented. This cave is located in Podere Fainello (Ficulle, Italy) and is shown in Figure 1. It is at least four decades old, 6.3 m deep, 4.2-5.5 m wide and 2.7 m high (Figure 2), stable and self-supported.

(a) (b)

Figure 1: Podere Fainello excavated cave (a) Front view of cave entrance, and (b) Inside view of cave

Considering the self-supporting characteristic of the cave, the shear strength criteria of the soil should be characterised by a cohesive term to allow for the cave to be stable. However, strikingly, the material can easily be removed if scratched from the inner walls of the cave and it appears to be granular (cohesionless) at the touch.

The obvious questions that follow these findings are: what is generating cohesion in this material? Could the material be naturally cemented? Could suction be playing a role in the bonding of the soil particles?

This paper addresses experimentally, analytically, and numerically these questions. The prospects of cementation and suction acting as stabilising actors are investigated. If the material is cemented, this should appear macroscopically in intact samples in direct shear, when suction is relieved. Cement agents should also emerge from microstructure analyses. On the other hand, if stability is ensured by suction, it should be demonstrated that suction is sufficient to stabilise the cave when the shear strength criteria is formulated in unsaturated range and then implemented in stability analyses.

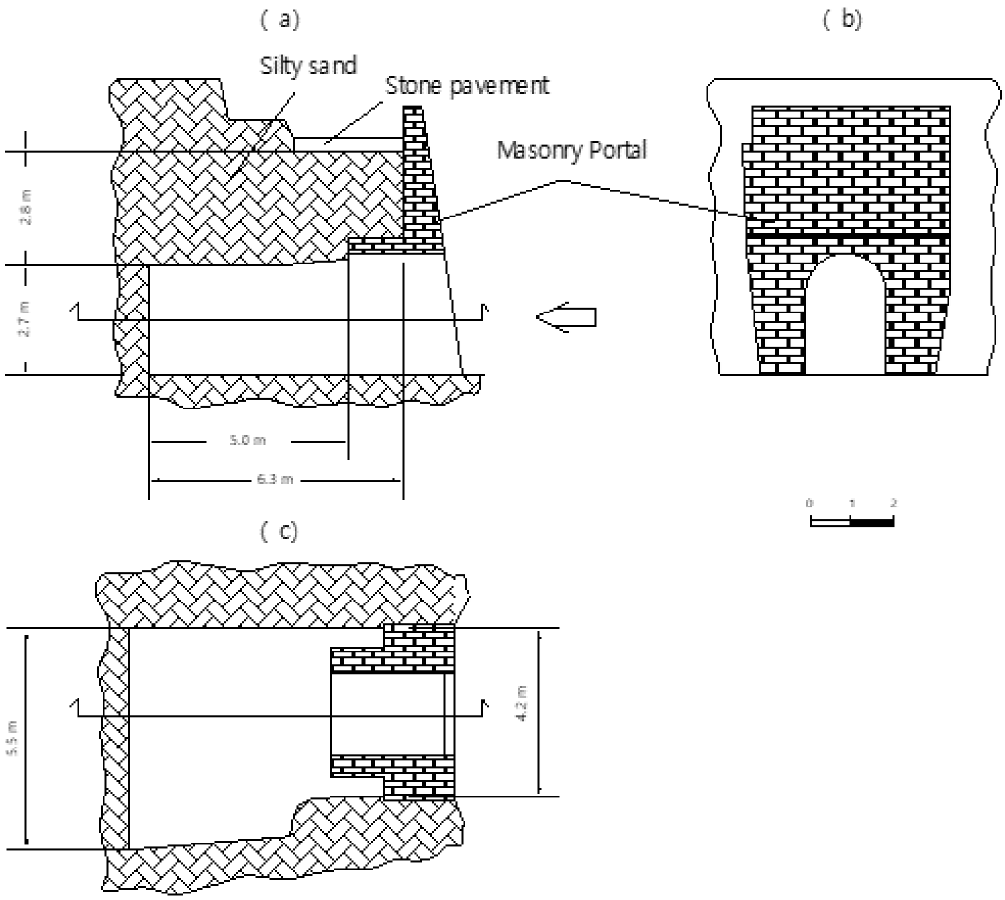

Figure 2: Podere Fainello excavated cave (a) vertical cross section, (b) front view, and (c) horizontal cross section.

2. Material

A few disturbed samples collected in October 2016 at different points along the internal walls of the cave indicated that the water content in the field ranged from 0.07 to 0.11. A couple of intact blocks were also collected at the site. A specific gravity of 2.62 was determined by the pycnometer method. The density and void ratio of the intact samples ranged from 1.89 to 2.03g/cm^3, and 0.34 to 0.48 respectively. The degree of saturation determined from samples collected from the cave fell between 0.44 and 0.65.

Figure 3 presents the particle size distribution of the soil carried out by wet sieving and sedimentation tests. According to the Unified Soil Classification System (USCS) the soil is then classified as Silty Sand (SM).

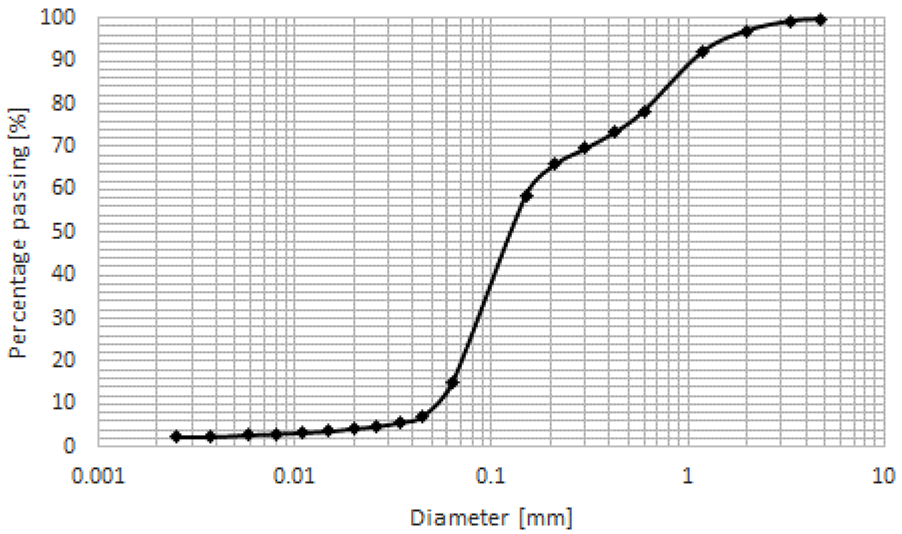

Figure 3: Grain size distribution of Podere Fainello soil, wet sieving and sedimentation

3. Investigating the hypothesis of cementation

3.1. Microstructure investigation

According to Sitar et al. (1980) the most common cementing agents naturally found are: silica, calcium carbonate, clay minerals and iron-bearing minerals. X-ray diffraction (XRD) result carried out on a soil sample collected from Podere Fainello cave is shown in Figure 4. The XRD result indicated the presence of mainly three minerals: quartz, calcite and kyanite. Further tests of simple loss of ignition (Heiri et al. 2001) demonstrated that the soil has 16% of calcium carbonate in its composition, which is associated with calcite. Thus, the question that followed was whether the calcium carbonate forms individual particles or the bonding between particles.

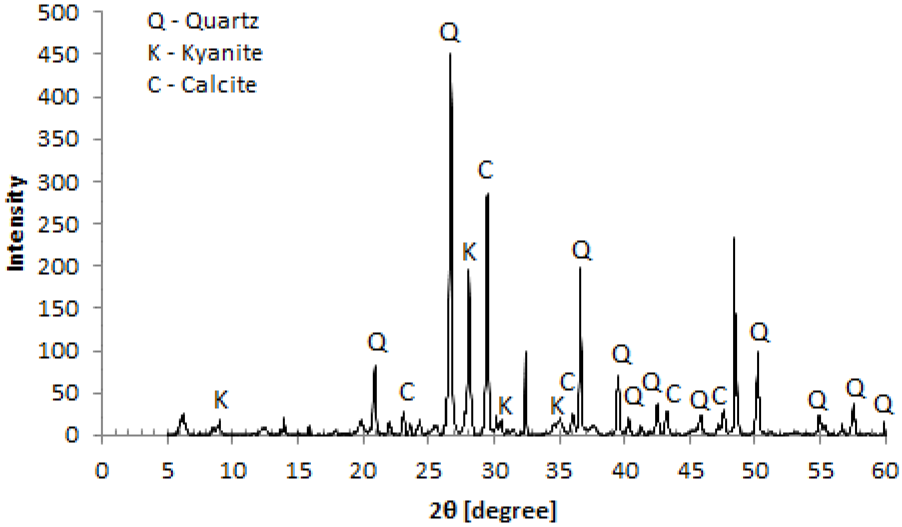

Figure 4: XRD data, Podere Fainello soil sample

The soil in question is found in a region of sedimentary rocks from late and post-orogenetic marine and continental deposits and alpine and continental plio-quartenary deposits (SELCA 2005). The presence of seashells is visible to the naked eye. Shells are almost entirely made of calcium carbonate (DOE 2016), in the mineral form of calcite or aragonite (Deckker et al. 2016). Since the XRD result of the soil sample indicated on one hand the presence of calcite and on the other the absence of aragonite, clearly at least some of the calcium carbonate in the form of calcite identified in the tests are coming from the seashells. Thus, further investigation was needed to determine if the calcium carbonate identified refers to the presence of seashells alone, or is derived from seashells together with cementing agents.

The thin section in Figure 5 shows the minerals identified in the XRD test. However, it is not possible to observe bonding between particles. Thus, an approximately 5mm soil sample was subjected to 3-D X-ray computed tomography (XCT).

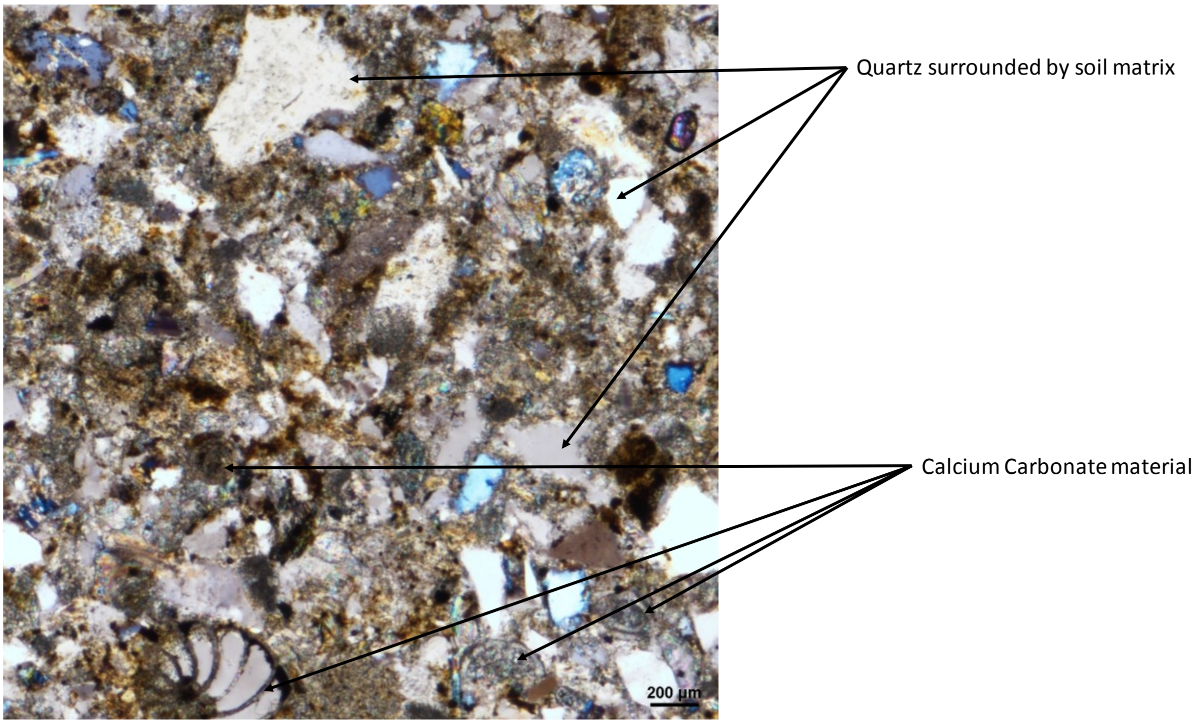

Figure 5: Thin section image, Podere Fainello soil sample

XCT is an approach that uses X-ray similar to conventional X-ray radiography, generating a set of object radiographs that reveal hidden internal structures (Wilson et al. 2018). The grey values that represent the relative X-ray attenuation are a product of a number of material properties, such as its density, chemical composition, and thickness. Kyanite has density of 3.61 g/cm^3 while quartz and calcite have very close densities, 2.65 and 2.71g/cm^3, respectively. Additionally, some other calcium carbonate phases have different ranges of densities that may be distinguished from calcite in the XCT. Therefore, if the calcium carbonate phase of the seashells has density different from the supposed calcium carbonate phase of the cementing agent, then it could be detected in the XCT scan.

Figure 6a shows a cross section of the generated volume. In this image, it is possible to notice the presence of seashells, as well as materials of varying shades of grey. There are a few areas where the grey scale value is very high (around 13,000), area delimited by blue rectangle, that indicates high attenuating value, possibly kyanite, in contrast, voids are indicated by black areas. It is also possible to measure the grey scale value (around 9,770) related to the region where there is strong evidence of the presence of seashells (area delimited by red rectangles).

(a)

(b)

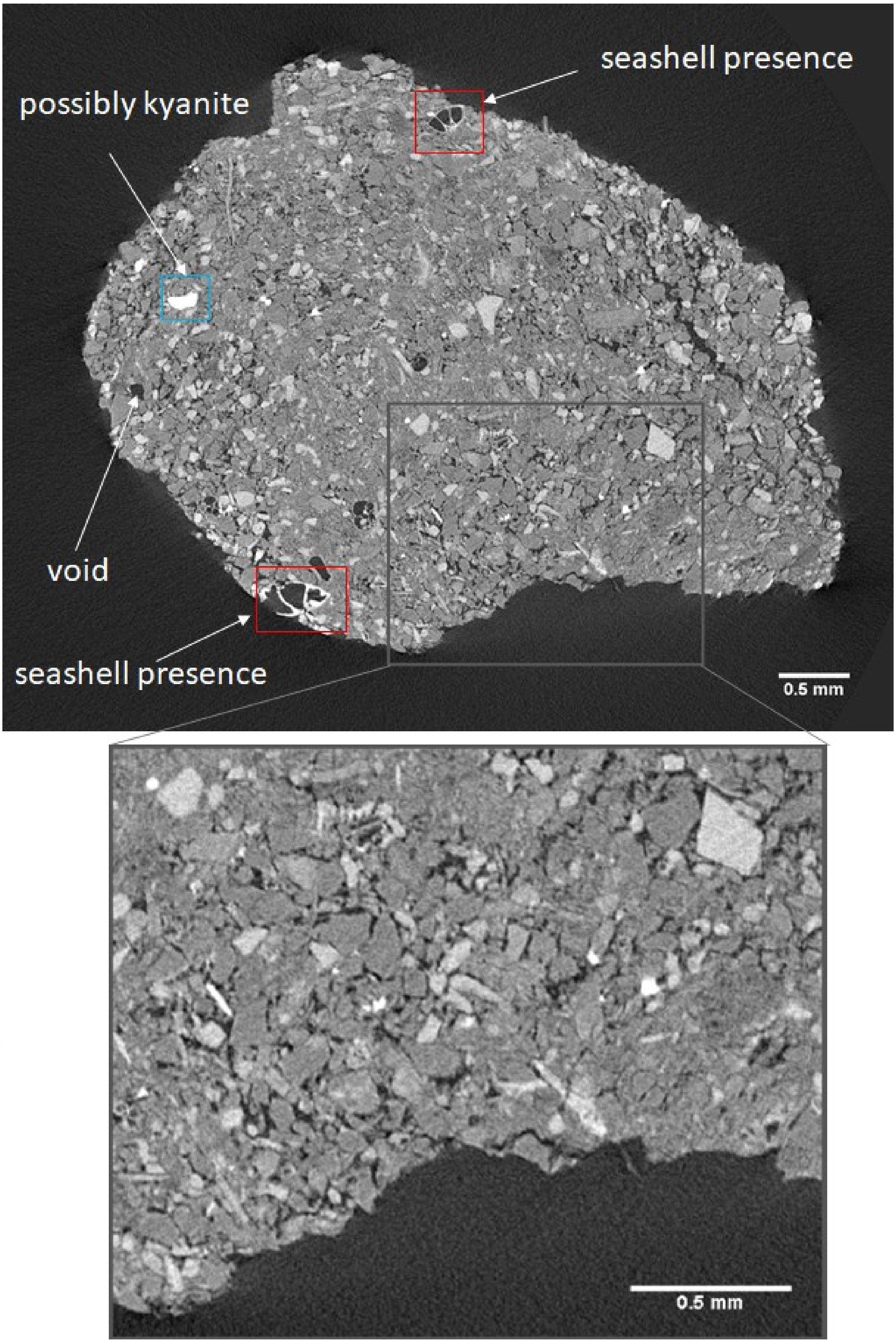

Figure 6: XCT cross section image, Podere Fainello soil sample. (a) Blue rectangle delimits the area with very high grey scale values, red rectangles delimit the area where there is strong evidence of the presence of seashells (b) zoom in grey rectangle area.

Figure 6b shows the magnification of a section of Figure 6a. An extensive part of this image shows detached grains, which could contribute to the argument of the inexistence of cementing bonds. Meanwhile, there are areas in Figure 6 in which the absence of links between particles is less obvious. Nevertheless, it is equally important to emphasise two points: 1) Figure 6 is a cross section of the 3-D XCT test, therefore that are other planes below this cross section that could be seen in the image, and 2) the scale could also be contributing to the hardship of identifying smaller single particles.

In Figure 7, the histogram of grey scale values for the sub volume of the tomogram shown in Figure 6a is presented. Let us now assume that the grey values associated with visible seashells is characterising all the seashells in the material. Thus, the grey values range associated with the voids and the calcium carbonate phase of the seashell are indicated in Figure 7.

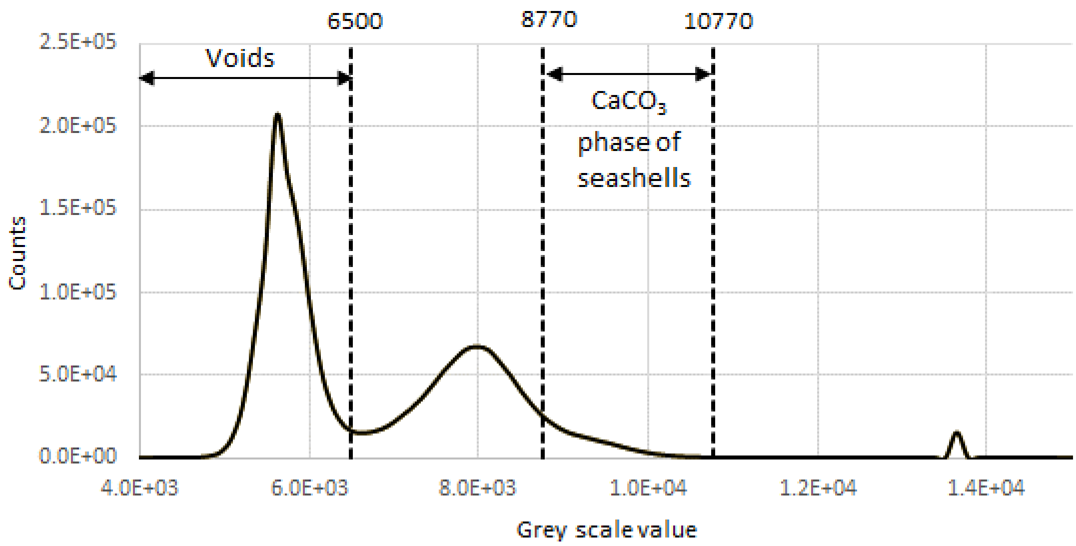

Figure 7: Histogram plot of grey scale values for a sub volume of the tomogram

Figure 8 was generated by filtering the grey scale value between 8,770 and 10,770, which should be related to the calcium carbonate phase of the seashells. The area occupied by the threshold seashell grey scale values in Figure 8 represents 15.1% of the total image area. If this approach is extended to the whole sample, this value reaches 15.4%, which is consistent with the value determined by the simple loss of ignition test (16%). This may suggest that most of the calcium carbonate identified are associated with seashells. Moreover, the shape of the material that is representative of the calcium carbonate phase of the seashells appears to form grains, not bridges between particles.

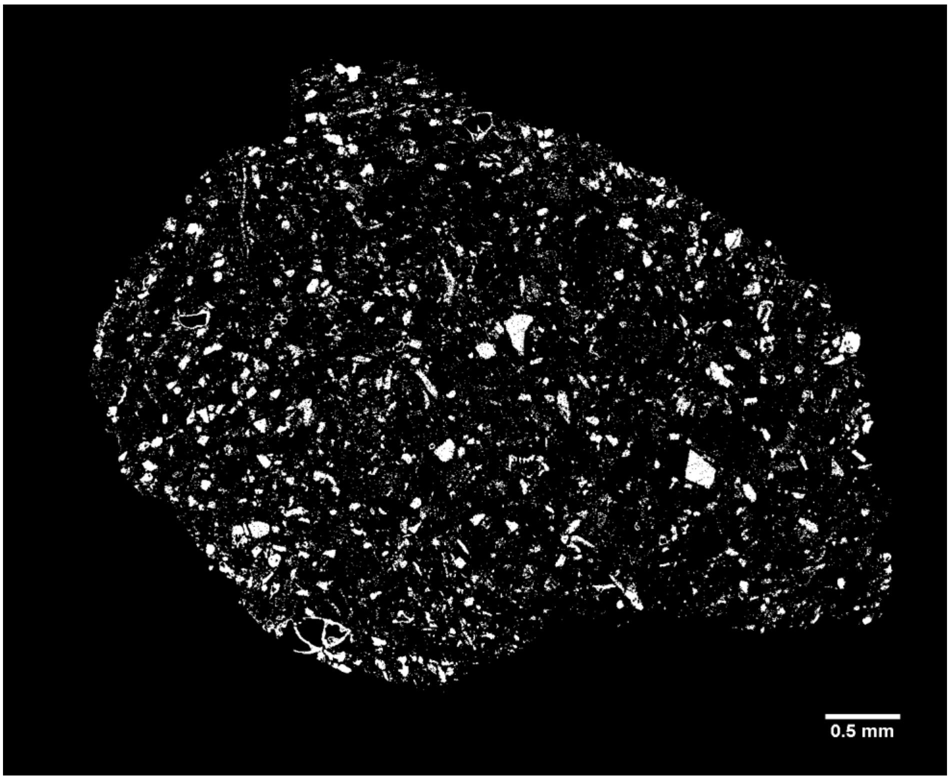

Figure 8: XCT cross section image with threshold densities around densities values found in the surroundings of seashell areas

3.2. Geomechanical investigation

The possible cementation was also investigated geomechanically by carrying out standard oedometer compression and direct shear tests on specimens either intact or reconstituted. The term reconstitute refers to the process in which the soil is dried in the oven at 105ºC for 24hrs, crushed using a mortar and pestle and mixed with distilled water (in this case the target water content was 30%) using a mixer. The reconstitution procedure is likely to break the bonding observed in naturally cemented materials (Burland 1990; Cuccovillo 1995), while the intact sample keeps the characteristics of the material in situ.

The oedometer compression test followed standard procedure, which means that both samples were flooded with distilled water for 24hrs before loading started and each loading stage was considered completed when primary consolidation was reached. Figure 9 shows the consolidation curve of both samples. The curves are identical up until 210kPa and then they diverge slightly from this loading stage up to 2100kPa. The unloading curves are parallel. Typical comparison between intact and reconstituted samples of cemented soils shows differences at lower and not high stresses (Cuccovillo 1995). The slight difference at high stresses observed here can be associated with the heterogeneity of the material in the block from which the specimens were taken from. The oedometer compression results then go in the direction that the natural soil is not cemented.

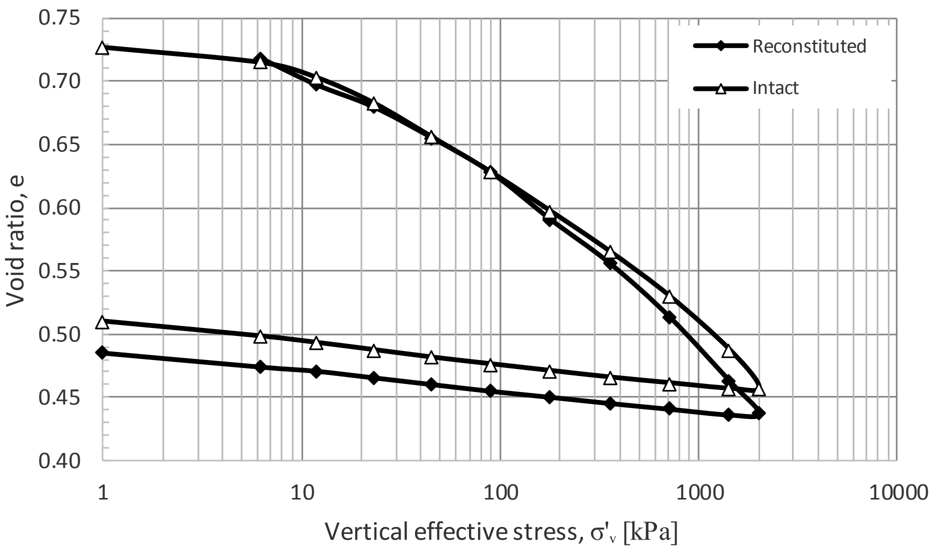

Figure 9: Reconstituted and intact consolidation curves of Podere Fainello soil specimens

Similarly, direct shear tests were carried out using sets of intact and reconstituted specimens (Figure 10). Again, specimens were flooded with distilled water for 24hrs before compression loading started. Shearing was imposed by a horizontal displacement rate of 0.065 mm/min, which ensured drained conditions. The shear strength envelope in both cases is not characterised by an effective cohesive term and the angles of internal friction found were essentially the same, 37° and 36° for intact and reconstituted specimens respectively. Again, the direct shear tests would suggest that the natural soil is not cemented.

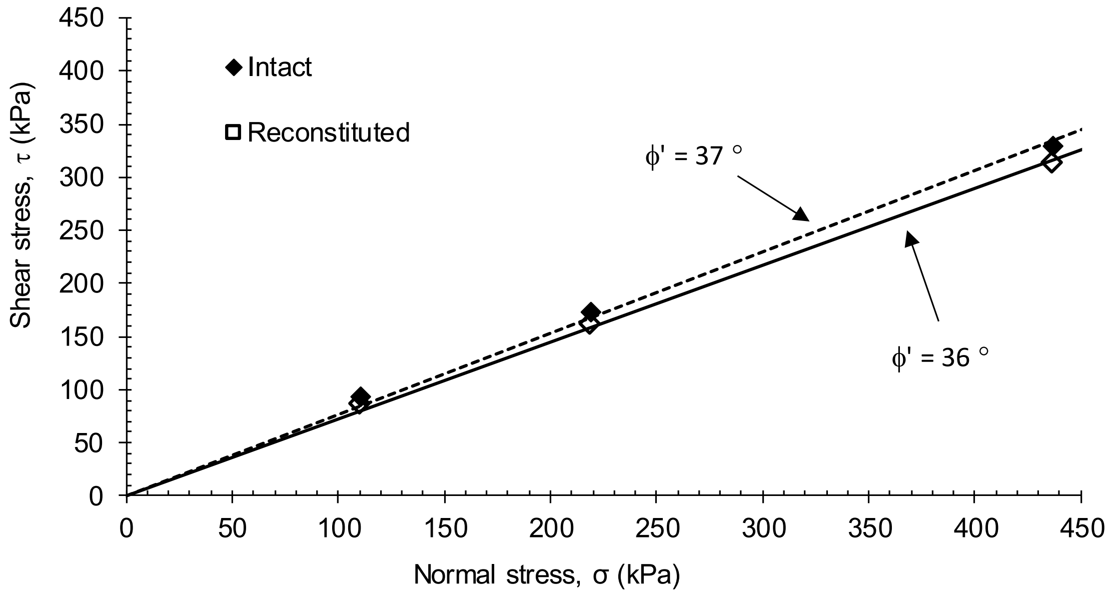

Figure 10: Reconstituted and intact shear strength failure envelope of Podere Fainello soil specimens under saturated conditions

The evidences presented here seem to corroborate with the fact that the calcium carbonate found in the soil in question comes from the seashells present in the soil and there are no other identified cementing agents (clay mineral, iron-bearing minerals) in the soil that can validate the hypothesis that the soil is naturally cemented.

Thus, the assumption that the capillary tension in the soil, which is found in the field unsaturated, could be acting as a stabilising agent in the cave was put forward to be further investigated. In fact, Sitar et al. (1980) acknowledged that capillary tension can produce similar effects to cementing agents, which could mislead one to believe that uncemented soils have cementing agents in their composition.

4. Investigating the hypothesis of suction generating apparent cohesion

4.1. Qualitative tests of specimens' dissolution in water

Two interesting facts were observed on the material from the cave. The silty sand can easily be removed if scratched from the inner walls of the cave. At the same time, samples crumble if placed in water as demonstrated in Figure 11.

Figure 11a shows a sample about 3cm in length. It was immersed in distilled water (no shaking or vibration took place) and left to stand, it crumbled completely after just a few minutes (Figure 11b), and water was visible clear 3 hours after immersion suggesting all the material had sedimented (Figure 11c). This observation seems to suggest that suction was holding the sample together and once it was saturated the menisci were lost and the sample crumbled.

In order to assess whether the size of the sample would play a role, a larger sample about 10cm in length (Figure 11d) was considered. It was immersed in distilled water in the same manner as the first sample. Seven days after immersion (Figure 11e) the water was visibly clear, the outer part of the sample had crumbled but the inner part remained resembling the original piece. The sub-sample was removed from the water (Figure 11f) and allowed to stand for 24hrs at environmental temperature (Figure 11g), then it was placed in an oven at 105°C for an additional 24 hours (Figure 11h). Upon retrieval form the oven the oven-dried sample was still intact. Subsequently, the oven-dried sample was immersed once again in water (Figure 11i). From the moment the sample was removed from water before placing it in the oven to the re-immersion in water, there has been no significant loss of material. Three hours after immersion, the sample had crumbled completely (Figure 11j).

These observations appear to indicate that the internal pores of the larger sample in Figure 11d were inaccessible to water reasonably due to air pockets remained entrapped between the water advancing from the outer surface of the sample and inner bulk water forming a continuous barrier within the sample. This entrapped 'cushion' of air would have prevented the water from flooding all the inner pores of the sample.

On the other hand, the oven would have removed all bulk water and possibly left just menisci at the inter-particle contacts. The water menisci, maintained at the inter-particle contact despite the oven-drying, would have been responsible for holding the silt particles together and allowing the sample to maintain the same shape as before the insertion in the oven. This point is discussed in more detail in Appendix 1 where additional experiments are presented to corroborate the assumption that water menisci are still present at the inter-particle contact following oven-drying.

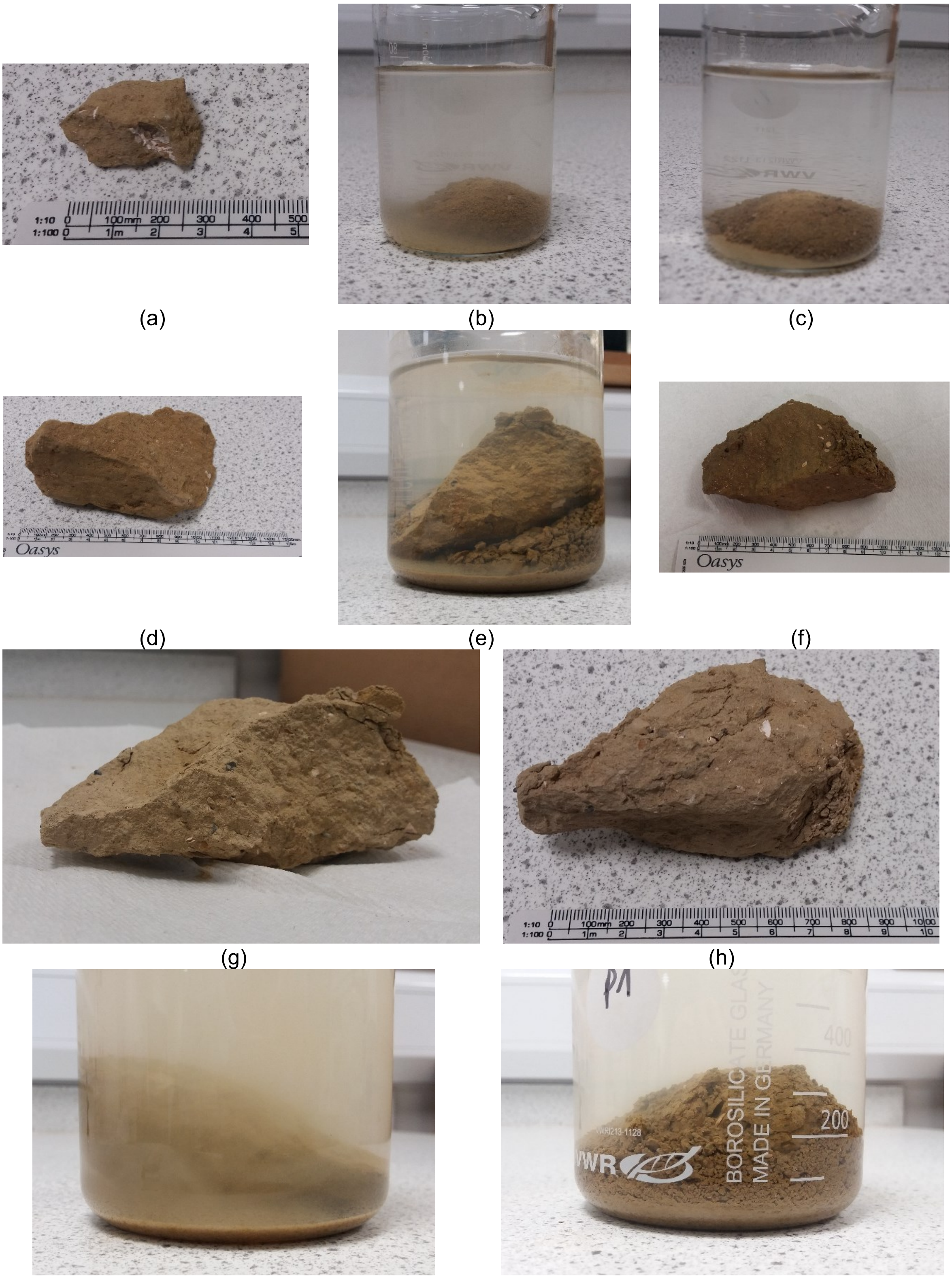

(a) (b) (c)

(d) (e) (f)

(g) (h)

(i) (j)

Figure 11: Podere Fainello samples immersed in distilled water (a) 3cm irregular sample at natural state, (b) 3cm sample a few minutes after immersed in water, (c) 3cm sample 3hrs after immersed in water, (d) 10cm irregular sample at natural state, (e) 10cm sample 7 days after immersed in water, (f) 10cm sample removal from water after 7 days, (g) 10cm sample air dried for 24hrs, (h) 10cm sample oven dried at 105°C for 24hrs, (i) 10cm sample a few minutes after re-immersed in water, and (j) 10cm sample after 3hrs re-immersed in water.

By removing all bulk water though the oven drying, the air would have been continuous in all sample pores before re-submersion in water and this would have allowed water to flood all pores, thus causing the entire sub-sample to crumble down.

4.2. Shear tests on intact samples under unsaturated conditions

Water-undrained direct shear tests were carried out on intact specimens under unsaturated conditions to assess the contribution of suction to shear strength and, hence, allow quantifying its contribution to the stability of the cave.

Two series of tests were carried out. In the first series, the suction of specimens were measured using HCT and these specimens were then placed in the shear box in their 'natural state' , i.e. as taken from the block sample and sheared at different values of normal total stress (specimens A to D in Table 1). In the second series of tests, specimens were taken from the block sample after this has undergone significant drying, wetted to target water contents using moistened filter papers placed at the top and bottom surfaces of the specimen, placed in the shear box, loaded to 437kPa vertical stress, and sheared at constant water content (horizontal displacement rate of 0.065 mm/min). Before loading, two High-Capacity Tensiometers (HCT) were installed through the loading cap specially designed for the installation of HCT according to Caruso and Tarantino (2004). A kaolin paste – approximately at the plastic limit – was applied on the HCT porous filter to ensure proper hydraulic continuity with the specimen. Suction was therefore measured throughout the test. Specimens were about 10mm high (~ 30 d_{50}) to approach the thickness of the shear band and make the degree of saturation measured globally representative of failure conditions. Details of this second series of tests are provided in Table 1 (specimens 1 to 3).

Table 1: Direct shear and SWRC characteristics (suction measured by HCT and *Sr* determined experimentally) of intact specimens subjected to constant water content direct shear

ID	Hydraulic path	$S_{r,initial}$	$s_{initial}$ (kPa)	σ (kPa)	τ (kPa)	Δτ (kPa)	$S_{r,failure}$	$s_{failure}$(kPa)
A		0.62	79	110	132	49		
B	Water content of block sample	0.54	115	219	228	63		
C		0.58	103	219	199	34		

D		0.61	83	437	375	46		
1	Wetted after drying to hygroscopic water content	0.40	139	437	406	77	0.76	152
2		0.19	681	437	420	91	0.30	472
3		0.49	78	437	428	99	0.69	170

The results of the constant water content direct shear tests are presented in Figure 12 in terms of the contribution of suction to shear strength $\Delta\tau$, which is given by

$$\Delta\tau = \tau - \sigma \cdot \tan\phi' \qquad [1]$$

where τ is the shear strength measured in the direct shear test, σ is the normal stress, and ϕ' the angle of shearing ultimate resistance determined on saturated specimens at zero suction (Figure 10). The experimental values of $\Delta\tau$ were then compared with the product

$$s \cdot S_r \cdot \tan\phi' \qquad [2]$$

where *s* is the suction and S_r is the degree of saturation. This product was first calculated for the values of *s* and S_r at failure (ultimate state) for the specimens of the second series (1 to 3 in Table 1 and solid symbols in Figure 12). It appears that contribution of suction to shear strength $\Delta\tau$ is adequately modelled by Equation 2. and that shear strength for this material can therefore be formulated as

$$\tau = \sigma \cdot \tan\phi' + s \cdot S_r \cdot \tan\phi' \qquad [3]$$

This is consistent with the model originally proposed by Öberg and Sällfors (1997) for granular materials (silty and sandy soils) and further validated by Tarantino and El Mountassir (2013) against a relatively large database.

The product given by Equation 2 was then calculated for the initial values of suction and degree of saturation (for all 7 specimens tested). As shown in Figure 12, estimating the shear strength using the suction and the degree of saturation prior to shearing leads to a (very) conservative estimation of shear strength.

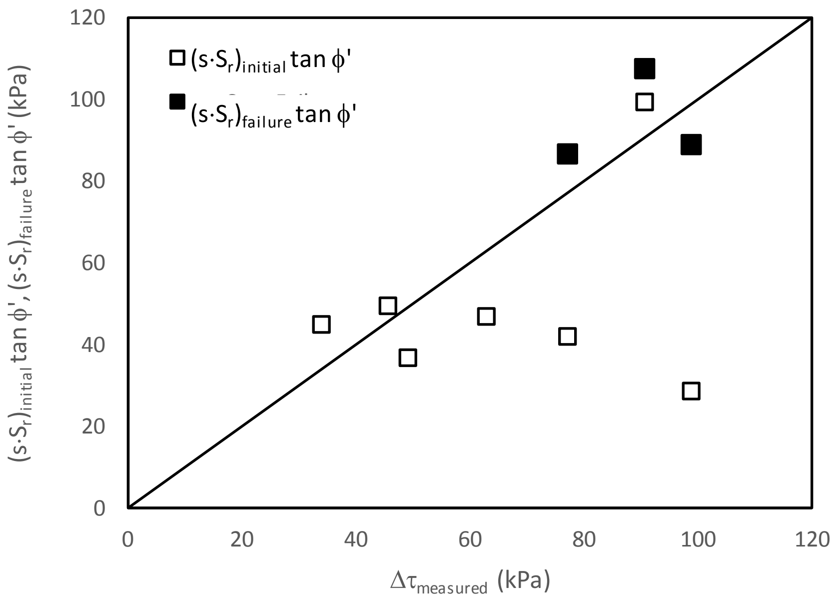

Figure 12: Contribution of suction to shear strength $\Delta\tau$: comparison between values measured and estimated based on initial and at failure degree of saturation and suction.

4.3. Stability analysis

The shear strength used to analyse the stability of the cave was estimated conservatively on the basis of the field (prior to shearing) suction and degree of saturation as follows

$$\tau = \sigma \cdot tan\phi' + \underbrace{(s \cdot S_r)_{field} \cdot tan\phi'}_{c_{suction}} \qquad [4]$$

where $c_{suction}$ is an apparent cohesion representing the contribution of suction to shear strength. If a single value of $c_{suction}$ is selected for the material in question, the stability analysis can be carried out by means of limit analysis.

To estimate s and S_r in the field, a water retention curve was derived experimentally for intact specimens cut from the block sample. Some specimens were air-dried and some specimens were wetted using moistened filter paper. The experimental data were fitted using the van Genuchten function (van Genuchten 1980).

$$S_r = \left[\frac{1}{1+(\alpha s)^n}\right]^m \qquad \left(m = 1 - \frac{1}{n}\right) \qquad [5]$$

where α, m and n are fitting parameters. Figure 13a shows the experimental data together with the correspondent van Genuchten fitting curve (α=0.079 kPa^{-1}, n=1.271, m=0.214). The air-entry suction for this material is s_{AE}~6 kPa.

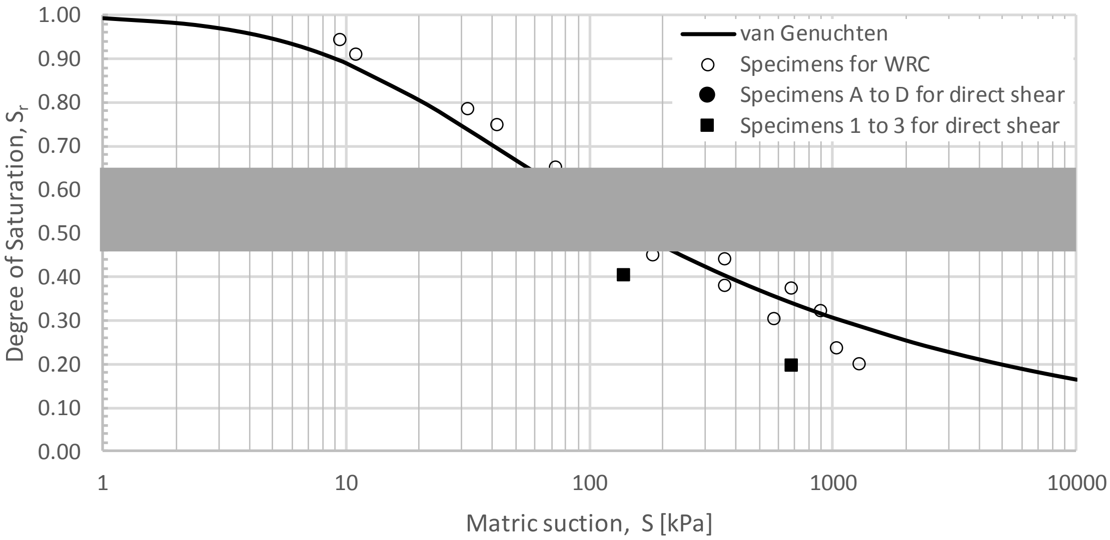

(a)

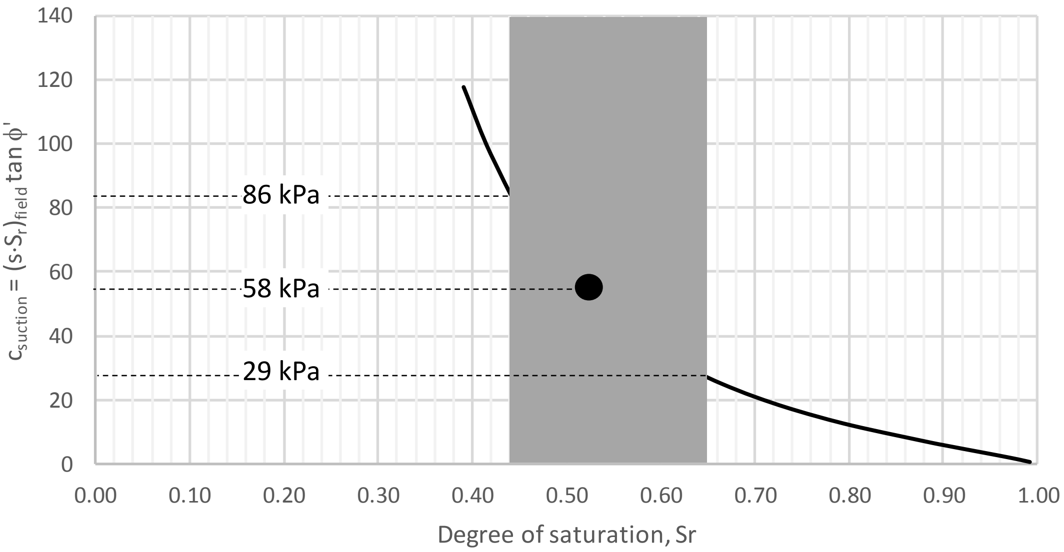

(b)

Figure 13: Podere Fainello soil. (a) Soil water retention curve, shaded area represents the range of degree of saturation found in the cave in October 2016, (b) Degree of saturation versus product of suction times degree of saturation times tangent of friction angle derived from van Genuchten fitting.

The degree of saturation determined from the water content measured in the field ranges between 0.44 and 0.65 as shown by the shaded area in Figure 13a. The corresponding value of $c_{suction}$ ranges between 29 and 86 kPa and an average value of 58 kPa was used to assess the stability of the cave roof (Figure 13b).

A 3-D analytical stability analysis of the roof of the cave, within the upper bound theorem of plasticity, was carried out. Thus, a kinematically admissible mechanism had to be considered. To be able to determine the 3-D mechanism more accurately, the problem was initially accessed in 2-D using Optum G2 software (Krabbenhoft et al. 2016), where the mechanisms minimising the difference between the works done by the internal stresses and the external forces is searched numerically using the Discontinuity Layout Optimization (Appendix 2). Additional 2-D numerical analyses were carried out in Optum G2 and also presented in Appendix 2.

Considering the 2-D solution, a simplified mechanism based on a single-block (B = 4.8m, L = 6.3m, H = 2.8m and ϕ' 37°) was considered for the 3-D stability analysis as shown in Figure 14. The faces of the block were designed to be inclined with respect to the vertical plane of an angle equal to the friction angle. In this way, an absolute displacement of the block directed vertically, as shown in Figure 14, returns a kinematically admissible mechanism.

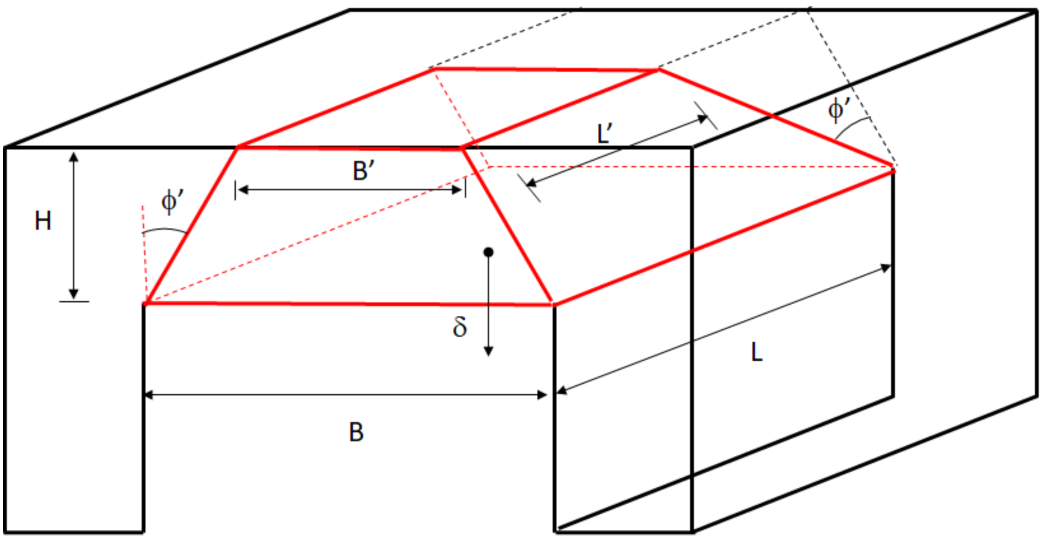

Figure 14: Single-block kinematically admissible mechanism for Podere Fainello cave (B = 4.8m, L = 6.3m, H = 2.8m, c=58 kPa, and ϕ' 37°)

With this kinematic mechanism, the (destabilising) work done by the external forces, W_e, can be written as follows:

$$W_e = W \cdot \delta \qquad [6]$$

where W is the weight of the block and δ is the displacement of the block directed vertically. The (stabilising) work done by the internal stresses, W_i, can then be written as:

$$W_i = c_{suction} \cdot A \cdot (\delta \cos\phi') \qquad [7]$$

where A is the area of the surface of the block where shear stresses are transmitted through the failure planes. Stability occurs if $W_i \geq W_e$. For the case shown in Figure 14 the work done by the internal stresses W_i was found to be greater than the work done by the external forces W_e (Table 2) and the cave is therefore stable within the assumptions of the upper bound theorem of plasticity.

Table 2: Factor of safety of the cave roof under hydrostatic conditions and following rainfall intensity of 144 mm/day and 82mm/day lasting for 1 and 2 days respectively for a return period of 100 years

	$s_{average}$ (kPa)	s.Sr [kPa]	γ [kN/m^3]	W_e [kN m]	W_i [kN m]	$\gamma_{\phi'}$ –
Hydrostatic	150	77			2141	2.09
1-day rainfall of 82mm/day	104	58	19	869	1573	1.65
2-day rainfall of 144mm/day	72	44			1188	1.32

The partial safety factor for the frictional strength, $\gamma_{\phi'}$, defined as the ratio between ultimate shear strength τ and the mobilised shear strength, τ_{mob},

$$\gamma_{\phi'} = \frac{\tau}{\tau_{mob}} \qquad [8]$$

is found to be equal to $\gamma_{\phi'}$=2.09 for the case shown in Figure 14.

The stability of the cave and its roof is therefore substantiated by this simple calculation. Suction can therefore be a powerful soil ‘reinforcement’ capable of maintaining stable a cave excavated in granular cohesionless material with flat roof.

It is then interesting to explore the effect of rainfall on the stability of the cave roof. Infiltrating rainwater tends to reduce suction and, hence, shear strength. In turn, this leads to a reduction of the factor of safety.

In order to determine the appropriate design rainfall to assess the stability of the cave, the rainfall data recorded by the meteorological station located in Ficulle, Italy (ServizioIdrografico 2019) was analysed using the double exponential probability distribution known as the Gumbel distribution. The Gumbel distribution curve is written as follows.

$$P(H < h;\ a, b) = e^{-e^{-\left(\frac{h-a}{b}\right)}} \qquad [9]$$

where H and h are precipitations in mm, a and b are Gumbel fitting parameters (for 24hrs rainfall a = 51mm, b = 21mm, for 48hrs rainfall a = 64mm, b = 22mm) and P(H<h; a, b) is the probability that precipitation H is smaller than h. Figure 15 shows the cumulative probability distribution function of the maximum precipitation with durations of 24 and 48hrs data series between 1920 and 2015 fitted with Gumbel distribution together with return period (T) curves for both precipitation durations derived from Gumbel distribution, knowing that:

$$T = \frac{1}{1 - P(H < h; a, b)} \qquad [10]$$

A return period of 100 years was considered representative and significant for the analyses since the cave has been stable for decades. Thus, two analyses were performed, taking as design intensity 144mm/day for 1 day and 82mm/day for 2 days (for a total of 164mm). These are extreme events if one considers, for comparison, that the rainfalls recorded over an entire year in 2015, 2016, 2017, and 2018, were 562, 469, 374, and 570mm respectively.

The water retention curve of the silty sand was assumed to be represented by the van Genuchten function shown in Figure 13a. The saturated hydraulic conductivity was assumed to be equal to k_{sat} = 10^{-7} m/s according to the measurement on an intact specimen via constant head water flow in the oedometer cell after pausing the compression test at the vertical stress of 100 kPa. The intact specimen was cut from the block using a cutting-edge oedometer ring, trimmed, placed in the oedometer cell, and saturated for 24h under a small vertical stress. The unsaturated hydraulic conductivity, k, was determined following Kozeny-Carman model (Mitchell and Soga 2005) with

$$k = k_{sat} \cdot S_r^3 \qquad [11]$$

Chapuis and Aubertin (2003) demonstrated that Kozeny-Carman equation provides good predictions of hydraulic conductivity of soil specimens, including silty sand materials. This model was preferred to the van Genuchten-Mualem function (van Genuchten 1980) because it overestimates the hydraulic conductivity compared to van Genuchten-Mualem model and therefore represents a conservative choice for the case where the simulation addresses the problem of loss of suction and, hence, shear strength due to rainfall.

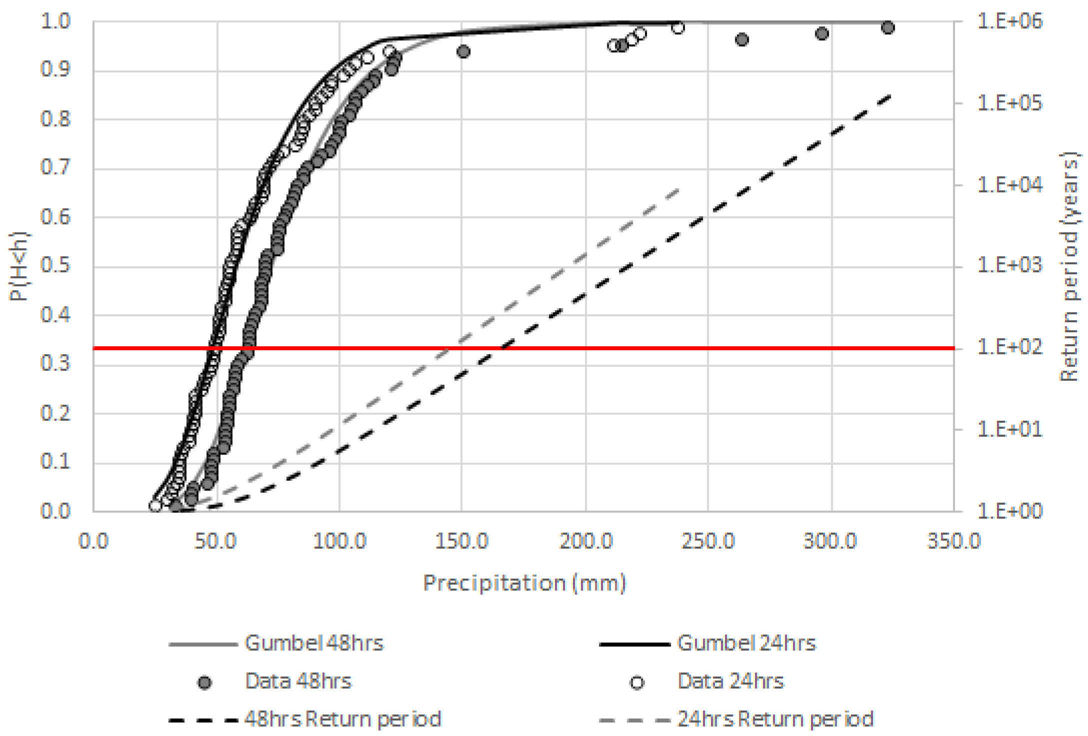

Figure 15: Cumulative probability distribution function of Ficulle 24 and 48hrs precipitation data series between 1920 and 2015: experimental data (ServizioIdrografico 2019) and Gumbel distribution fitting,

together with return period curves for 24 and 48hrs precipitations derived from Gumbel distribution. Horizontal red line indicates the return period of 100 years for which the analyses were carried out.

The water flow partial differential equation was solved via a numerical code based on the Finite Element Method, under transient analysis. The mesh consisted of 181 nodes and 273 elements, the boundary condition at surface were water flux equivalent to the design rainfall considered.

The boundary condition imposed on the cave walls consisted of zero flux if pore-water pressure is negative (positive suction) with the condition that pore-water pressure can never attain positive values. This condition is not realistic because ventilation in the cave tends to generate outward flux and therefore lower degrees of saturation in the soil surrounding the cave. However, this boundary condition is conservative for the case where the simulation addresses the problem of loss of suction and, hence, shear strength due to rainfall.

The initial pore water pressure distribution was assumed to be hydrostatic with the ground water table at 16.4m below the cave roof. The ground water table depth was estimated based on water content behind the cave walls and the water retention curve determined in the laboratory on intact samples. Since the rainfall regime consists of intense rainfalls with long intermittent dry periods, the pore-water pressure profile would be characterised by values lower than hydrostatic. Again, an initial hydrostatic pore-water pressure distribution would therefore be conservative for the case where the simulation addresses the problem of loss of suction and, hence, shear strength due to rainfall.

The pore-water pressure profiles within the cave roof after 1 and 2 days of constant rainfall of 144 mm/day and 82mm/day respectively are shown in Figure 16. Pore-water pressure becomes less negative (suction decrease) in the upper part of the cave roof. However, the partial safety factor, $\gamma_{\phi'}$, remains relatively high (FoS=1.32).

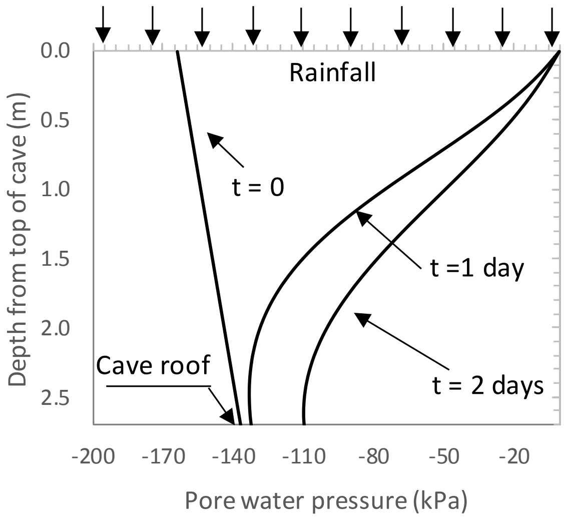

Figure 16: Effect of a rainfall of 144 and 82mm/day for 1 and 2 days respectively on the pore water pressure profile throughout the cave roof. Profiles t = 0, t = 1 day and t = 2 days correspond to hydrostatic condition, 24 hours after the 1-day rainfall event of 144mm/day and 48 hours after the 2-day rainfall event of 82mm/day respectively.

Although the calculations presented in Table 2 should be regarded as approximate analyses of the stability of the cave roof, the fact that the partial safety factor remains relatively high even for the case of 2-day rainfall supports the assumption that suction generated in the silty sand is sufficient to ensure long-term stability of the cave.

The upper bound solution of limit analysis used for the three-dimensional analysis of the stability of the cave roof has a number of limitations due to the assumptions underlying this method. The role of these assumptions is investigated in this Appendix 2.

The upper bound theorem of limit analyses returns a non-conservative value of the factor of safety that may be in principle very far from ‘exact’ solution. The ‘quality’ of the upper bound solution based on single-block kinematically admissible mechanism was investigated in 2-D by comparison with upper and lower bound solutions derived numerically based on a 2-D computational limit analysis approach. As discussed in Appendix 2, the single block upper bound solution in 2D is affected by an error in the range 6%-8%. It was considered reasonable to assume that similar error would be associated with the single block upper bound solution in 3-D, which was considered acceptable for the purpose of this analysis.

Possible arching effects were addressed in a simplified manner. The geometrical effect on arching was investigated by increasing fictitiously the thickness of the cave roof. As shown in the appendix, an arching effect clearly appears if the thickness becomes sufficiently large and this generates higher FoS.

Heterogeneous stiffness could be induced by the 1-D rainwater infiltration. Suction is reduced upon infiltration in the top layer of the soil profile (Figure 16) and this would make the top layer more deformable than the underlying regions. To investigate the effects of heterogeneous stiffness on arching, an analysis was performed where the Young modulus of the top layer was 'relaxed', i.e. the Young modulus was decreased by two orders of magnitude in the FEM analysis.

The failure mechanism does not change mainly because the decrease in stiffness affects the entire top soil layer, which encompasses the cave roof and the 'pillars' supporting the cave roof. In other words, the 1-D infiltration generates a 1-D deformation which does not produce an arching effect.

Finally, it should be highlighted the non-conservative nature of the upper bound solution is compensated by a number of conservative assumptions made in the characterisation of the material (shear strength and hydraulic conductivity in the unsaturated range), the assumptions about the hydraulic initial condition and the boundary condition on the inner wall of the cave, and the assumption that the top of the cave was considered bare, where in reality it is known that this area is vegetated, which reduces rainfall infiltration into soil above the cave.

5. Conclusion

This paper has assessed the long-term stability of a cave excavated in granular cohesionless soil in the region of Ficulle, Italy. Surprisingly, in the field, the material appeared to be granular (cohesionless) at the touch as it could be easily removed if scratched from the inner walls of the cave. In addition, soil samples easily crumbled down if submerged in water. The composition of the soil was investigated microstructurally, by means of XRD, thin section and XCT, as well as by geomechanical standard testing. Both approaches produced enough evidence to suggest that the material in question is not naturally cemented. On the other hand, water-undrained direct shear tests on intact unsaturated samples indicated the presence of apparent cohesion, which was linked to the existence of suction in the material.

The stability analysis of the cave in Podere Fainello (Ficulle, Italy) was performed by limit analysis, accounting for the beneficial effects of suction and partial saturation on shear strength through an apparent cohesion term. The outcome of the analysis confirmed the stability of the cave over a notable high factor of safety.

The impact of rainfall on infiltration and cave stability was then explored. The 100 years' period of return was considered for two scenarios of design rainfall intensities of 24 hours and 48 hours' durations. Considering the top of the cave bare rather than vegetated, a conservative appraisal of cave stability was generated. The impact of 1 and 2 days of constant rainfall has been demonstrated to have no impact upon the cave stability. This would explain the long-term stability of Podere Fainello cave.

Suction is rarely included in geotechnical design under the assumption that it cannot be relied on due to the potential adverse effect of rainwater infiltration. This case study demonstrates that suction can indeed naturally remain 'active' for long periods of time contributing to the long-term stability of geo-structures.

Acknowledgements

The authors would like to thank Sergio and Francesco Leo for providing samples of the Silty Sand material and for allowing researchers access to the cave. The authors would also wish to acknowledge the contribution of Derek McNee, technician of the Geomechanics lab, who helped preparing the intact samples, Dr Alice Macente, X-Ray CT manager of the XCT equipment at the Advanced Materials Research Laboratory of University of Strathclyde, for scanning the intact sample and Laís de C.F.L. Lopes for helping with the experiments.

References

Burland JB (1990) On the compressibility and shear strength of natural clays. Géotechnique 40:329–

378

Caruso M, Tarantino A (2004) A shearbox for testing unsaturated soils at medium to high degrees of saturation. Geotechnique 54:281–284. https://doi.org/10.1680/geot.2004.54.4.281

Chapuis RP, Aubertin M (2003) Predicting the Coefficient of Permeability of Soils Using the Kozeny-Carman Equation

Cuccovillo T (1995) Shear behaviour and stiffness of naturally cemented sands. City University London

Deckker P de, Reeves J, Prendergast A (2016) She sells sea shells... Aust. Acad. Sci.

DOE (2016) How seashells get their strength. SienceDaily

Fisher RA (1926) On the capillary forces in an ideal soil; correction of formulae given by W. B. Haines. J Agric Sci 16:492–505. https://doi.org/10.1017/S0021859600007838

Heiri O, Lotter A, Lemcke G (2001) Loss on ignition as a method for estimating organic and carbonate content in sediments. J Paleolimnol 25:101–110. https://doi.org/10.1017/CBO9781107415324.004

Knight L (2003) Caves and caverns: stability

Krabbenhoft K, Lymain AV, Krabbenhoft J (2016) OptumG2. 85p

Mitchell JK, Soga K (2005) Fundamentals of Soil Behavior, Third Edit. John Wiley & Sons, INC

Öberg AL, Sällfors G (1997) Determination of Shear Strength Parameters of Unsaturated Silts and Sands Based on the Water Retention Curve. Geotech Test J 20:40–48. https://doi.org/10.1520/gtj11419j

Peck A, Halterman D (2019) Classification of Soils for Excavations

SELCA (2005) Geological map of Italy

ServizioIdrografico (2019) Regione Umbria. http://www.regione.umbria.it/ambiente/servizio-idrografico. Accessed 20 Aug 2019

Sitar N, Clough GW, Bachus RG (1980) Behaviour of weakly cemented soil slopes under static and seismic loading conditions

Stanier SA, Tarantino A (2013) An approach for predicting the stability of vertical cuts in cohesionless soils above the water table. Eng Geol 158:98–108. https://doi.org/10.1016/j.enggeo.2013.03.012

Tarantino A (2013) Basic Concepts in the Mechanics and Hydraulics of Unsaturated Geomaterials. ,. In: Laloui L (ed) Mechanics of Unsaturated Geomaterials

Tarantino A, El Mountassir G (2013) Making unsaturated soil mechanics accessible for engineers:

Preliminary hydraulic-mechanical characterisation & stability assessment. Eng Geol 165:89–104. https://doi.org/10.1016/j.enggeo.2013.05.025

Thompson LJ, Tanenbaun RJ (1975) Excavations, Trenching and Shoring: The Responsibility for Design and Safety. Texas

van Genuchten M (1980) A Closed-form Equation for Predicting the Hydraulic Conductivity of Unsaturated Soils. Soil Sci Soc Am J 44:892–898. https://doi.org/10.2136/sssaj1980.03615995004400050002x

Wilson PF, Smith MP, Hay J, et al (2018) X-ray computed tomography (XCT) and chemical analysis (EDX and XRF) used in conjunction for cultural conservation: the case of the earliest scientifically described dinosaur Megalosaurus bucklandii. Herit Sci 6:1–14. https://doi.org/10.1186/s40494-018-0223-0

Appendix 1. Stability of granular materials following oven-drying

This annex provides an explanation for the reason why the silty geomaterial investigated in this paper is extracted from the oven in the form of apparent aggregates after being placed moistened into the oven. Let us consider first the case of free water in a container placed in an ambient at relative humidity lower than 100% and ambient temperature T_{amb}. Because water vapour pressure at the air-water interface p_{v0} is greater than the ambient vapour pressure $p_{v\infty}$ (Figure 17), water is removed from the container. As evaporation proceeds, the air-water interface remains flat, and the water vapour pressure at the air-water interface maintains the value p_{v0} associated with the temperature T_{amb} on the vaporisation curve of the phase diagram of water. Because the vapour pressure differential remains constant, evaporation process only stops when there is no longer water in the container.

This process remains essentially the same if the container is placed in an oven at 105°C. The only difference is that the higher saturated vapour pressure on the vaporisation curve p_{v0} and the lower ambient vapour pressure in the oven $p_{v\infty}$ generate faster evaporation (because of the higher vapour pressure differential).

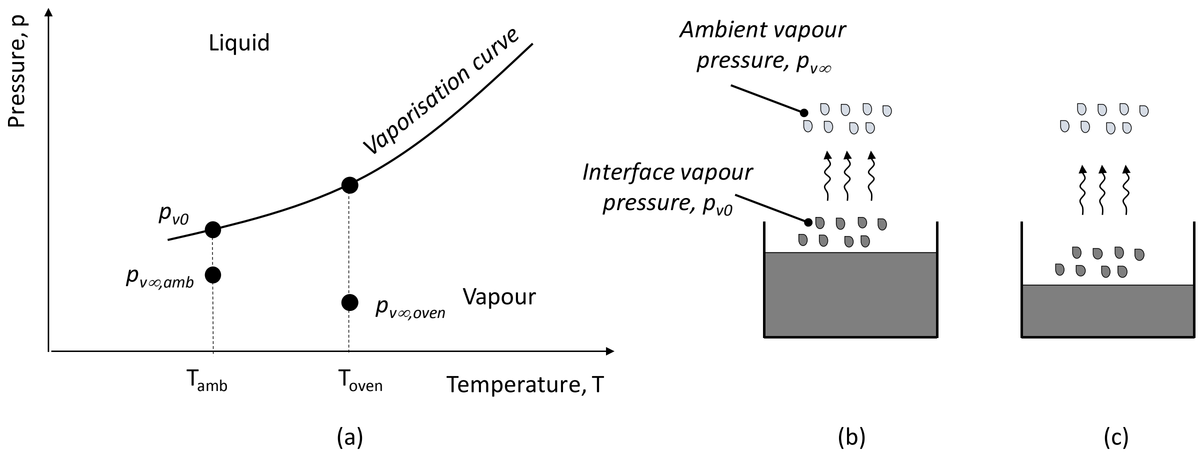

Figure 17: Evaporation from free liquid (flat air-liquid interface). (a) phase diagram for flat air-liquid interface. (b) vapour pressure gradient driving water removal by evaporation. (c) configuration of air-liquid interface as evaporation proceeds.

Let us now consider the case where evaporation occurs at the meniscus forming at the inter-particle contact between two spherical particles (Figure 18). Because the air-liquid interface is not flat, liquid pressure is lower than atmospheric and this causes a depletion of the saturated vapour pressure p_v according to the psychometric law (Tarantino 2013).

$$p_v = p_{v0} \exp\left[-\frac{v_l}{RT}\left(p_{air} - p_{liquid}\right)\right] \qquad [12]$$

where p_{vo} is the saturated vapour pressure associated with a flat air-water interface, R is the gas constant, v_l the liquid molar volume, T is the absolute temperature, and p_{air} and p_{liquid} are the pressure of air and liquid respectively. This implies that the vaporisation curve moves downward (Figure 18a). As evaporation proceeds, the meniscus recedes more, liquid pressure becomes more negative and the vaporisation curve keeps shifting downward eventually ‘catching’ the ambient vapour pressure $p_{v\infty}$, at which stage evaporation stops. At ambient temperature, the residual water content at the inter-particle contact due to capillary forces is referred to as hygroscopic water content. The same mechanism occurs in the oven, with the only difference that ambient vapour pressure in the oven is likely to be lower and the meniscus has to recede more for the vaporisation curve to catch the ambient vapour pressure $p_{v\infty}$.

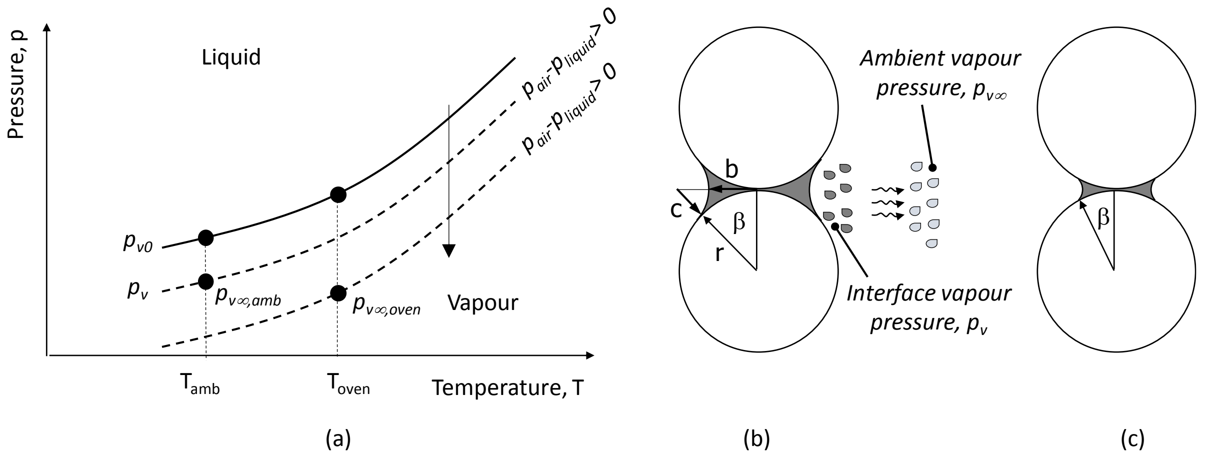

Figure 18: Evaporation from meniscus water at intergranular contact (air-water interface with increasing curvature). (a) phase diagram for flat air-liquid interface. (b) vapour pressure gradient driving water removal by evaporation. (c) configuration of air-liquid interface as evaporation proceeds.

As the meniscus recedes, liquid pressure changes significantly but the inter-granular stress at the inter-particle contact does not vary significantly. According to Fisher (1926), the inter-granular stress σ_i is given by:

$$\sigma_i = \frac{4T}{d\left(1 + \tan\frac{\beta}{2}\right)} \quad [13]$$

where d is the diameter of the spherical particle, T the liquid surface tension, and β is the angle defining the position of the air-solid-liquid junction (Figure 18b). A very simple exercise is shown Figure 19 where the inter-granular stress is plotted versus the angle β for the case of a silt and a sand particle (d_{silt}=20μm and d_{sand}=200μm) and two different liquid, water and acetone respectively (T_{water}=0.072 N/m and $T_{acetone}$ = 0.025 N/m). The inter-granular stress is higher for higher surface tension (water) and smaller particle size (silt).

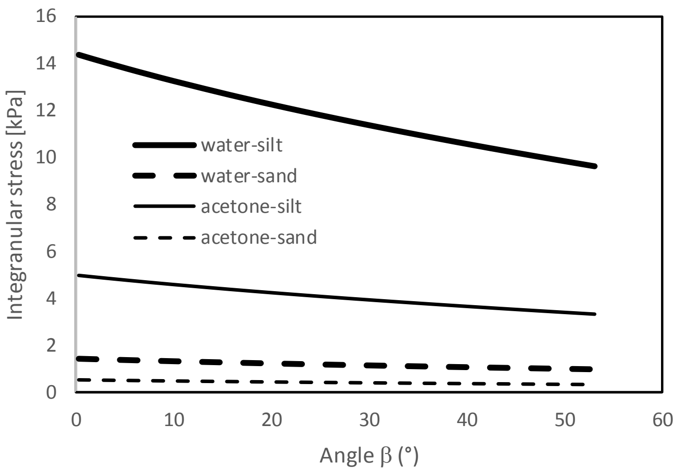

Figure 19: Integranular stress for different combinations of grain size and pore-fluid (d_{silt}=20μm, d_{sand}=200μm, T_{water}=0.072 N/m, $T_{acetone}$ = 0.025 N/m)

A very simple experiment was then carried to corroborate the outcome presented in Figure 19. Two dry granular powders were considered, the silty sand from Podere Fainello and a silica fine sand (Figure 20a,b). These were mixed with either demineralised water or acetone, placed on a Petri dish and inserted in the oven. Upon retrieval from the oven, the Petri dish was gently shaken and it was observed whether the material became ‘granular’. Results shown in Figure 20 are fully consistent with the inter-granular stress predicted by Equation [13] and shown in Figure 19.The finer-grained silty sand mixed with water does not ‘flow’ upon shaking (Figure 20e) in contrast to the coarser-grained sand mixed with the same water (Figure 20f). At the same time, the sandy silt easily breaks down when mixed with acetone (Figure 20c) in contrast with the same sandy silt when mixed with water (Figure 20e).

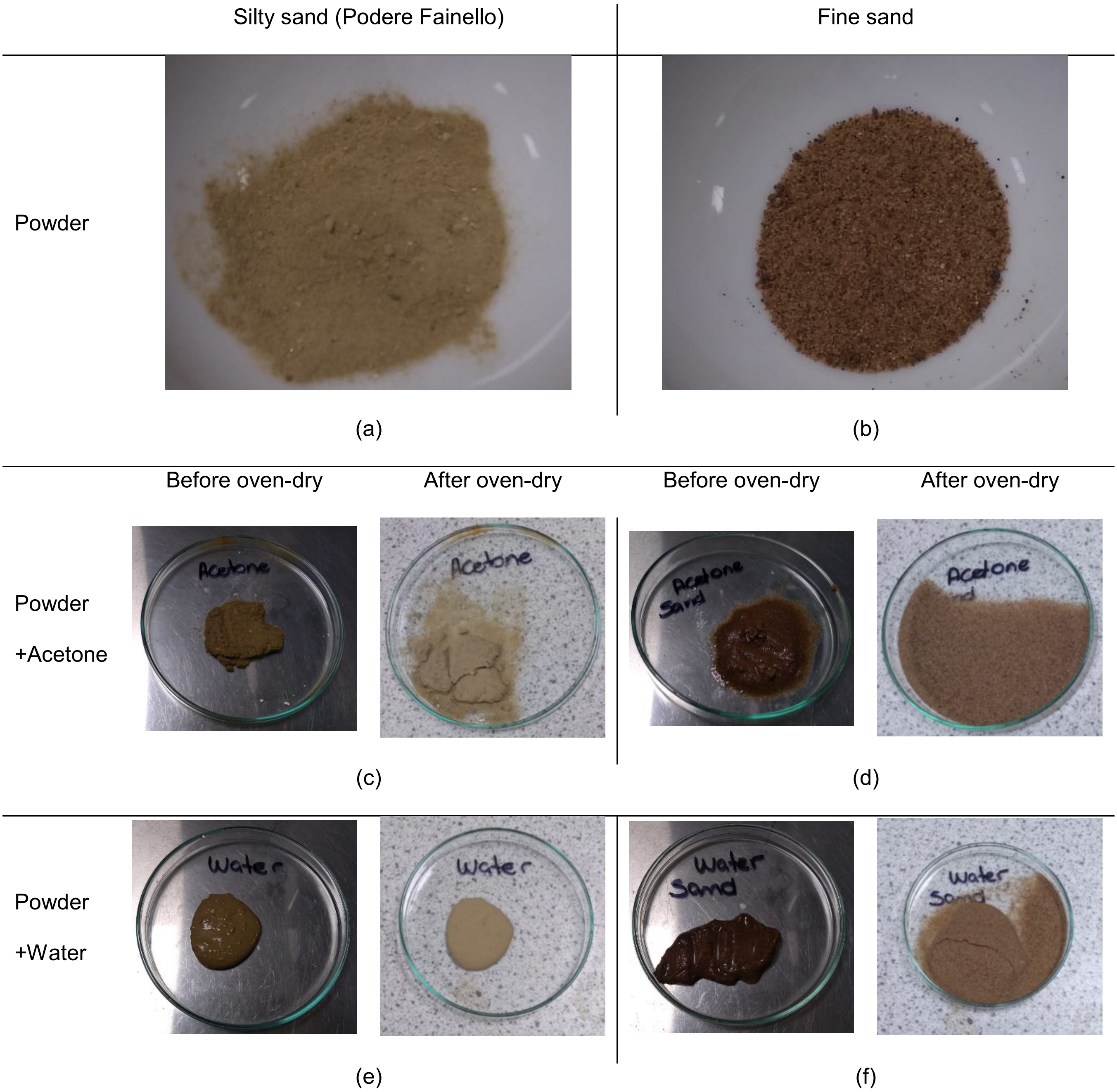

Figure 20: Effect of grain size and pore-fluid surface tension on stability of granular materials following oven-drying

Appendix 2. Two-dimensional analysis to explore limitations of the upper-bound solution

The upper bound solution of limit analysis used for the three-dimensional analysis of the stability of the cave roof has a number of limitations due to the assumptions underlying this method. The role of these assumptions is investigated in this Appendix by considering two-dimensional conditions. In particular, a 2-D upper bound solution was first derived by using single-block kinematically admissible mechanism, consistent with the one adopted for the 3-D analysis (Figure 21). Again, the shear strength criterion was defined by an angle of shearing resistance ϕ = 37° and a cohesion c = $c_{suction}$ = 58kPa. The unit weight was assumed equal to γ = 19 kN/m³. This upper bound solution returned a FoS = 1.81.

The 2-D stability of the cave was then investigated for comparison by using numerical upper and lower bound limit analysis and FEM analysis using elastic-perfectly plastic model.

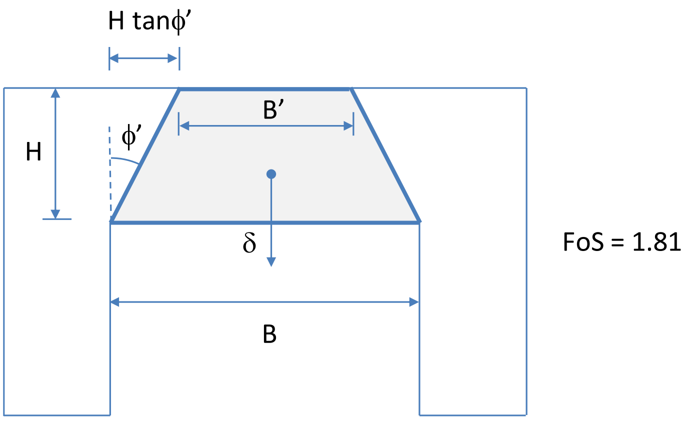

Figure 21: Single-block kinematically admissible 2-D mechanism for Podere Fainello cave (B = 4.8m, H = 2.8m, c=58 kPa, and ϕ' 37°)

Upper bound versus lower bound solution derived numerically

The upper bound theorem of limit analyses returns a non-conservative value of the factor of safety that may be in principle very far from the 'exact' solution. To investigate the 'quality' of the 2-D upper bound solution based on single-block kinematically admissible mechanism, upper and lower bound solutions of the stability of the cave were derived numerically based on a 2-D computational limit analysis approach via Optum G2 code (Krabbenhoft et al. 2016). The model created had 2000 elements and adaptive mesh refinement.

The 2-D upper bound solution derived numerically shows on a fan-type mechanism (Figure 22b), which is fairly consistent with the single block mechanism assumed for the 2-D analysis, This upper bound solution returned a FoS=1.7. On the other hand, the lower bound solution derived numerically using the Optum G2 code returned a FoS=1.64 (Figure 22a).

The 2-D exact solution could therefore be narrowly bracketed by these lower and upper bound values, i.e. 1.64<FoS<1.7. The upper bound solution based on single block in 2-D (FoS=1.81) is therefore affected by an error in the range 6%-8%. It was considered reasonable to assume that similar error would be associated with the single block upper bound solution in 3D, which was considered acceptable for the purpose of this analysis.

Table 3: Factor of safety derived from 2-D numerical analyses

Limit analysis			
Actual roof thickness		Augmented roof thickness	
Lower bound	Upper bound	Lower bound	Upper bound
1.64	1.7	1.7	1.8
FEM - Elastic-perfectly plastic model			
Homogenous stiffness		Heterogeneous stiffness	
1.64		1.64	

Geometrical and stiffness effects on arching

Arching may play a role in the failure mechanism and this is also investigated in this Appendix. The problem was not investigated in a rigorous way. This would have required a coupled analysis by implementing an appropriate constitutive model for the unsaturated material into a FEM code but this analysis was out of the scope of this paper. In addition, this would have required an extensive experimental campaign to calibrate/estimate the parameters of the constitutive model, which was again out of the scope of this paper.

Possible arching effects were addressed in a simplified manner. The geometrical effect on arching was investigated by increasing fictitiously the thickness of the cave roof. As shown in Figure 22c,d, an arching effect clearly appears if the thickness becomes sufficiently large and this generates higher

FoS. This also implies that the actual thickness of the cave roof is small to generate arching due to 'geometrical' effects.

Heterogeneous stiffness could be induced by the 1-D rainwater infiltration. Suction is reduced upon infiltration in the top layer of the soil profile (Figure 16) and this would make the top layer more deformable than the underlying regions. To investigate the effects of heterogeneous stiffness on arching, an analysis was performed where the Young modulus of the top layer was 'relaxed', i.e. the Young modulus was decreased by two orders of magnitude in the FEM analysis.

Figure 22e shows the case of the elastic-perfectly plastic model with the same strength parameters adopted in the limit analysis (c=58 kPa, and ϕ' 37°) and Young modulus and Poisson's ratio E = 11MPa and ν =0.35 respectively. The derive the Factor of Safety (FoS), the shear strength parameters were reduced manually by 0.01 until displacements became very high. Not surprisingly, the FoS value obtained for the EP FEM analysis returns the same value as the lower bound solution (FoS=1.64). The failure mechanism shown by the shear bands appears to be very similar to the one postulated in the single-block mechanism (Figure 21), corroborating the assumption made to derive analytically the singe-block upper bound solution.

Figure 22f shows the case of the elastic-perfectly plastic model with heterogeneous stiffness (E= 0.11 in the top layer and E = 11MPa in the rest of the region). The failure mechanism does not change mainly because the decrease in stiffness affects the entire top soil layer, which encompasses the cave roof and the 'pillars' supporting the cave roof. The 1-D infiltration generates a 1-D deformation which does not produce an arching effect.

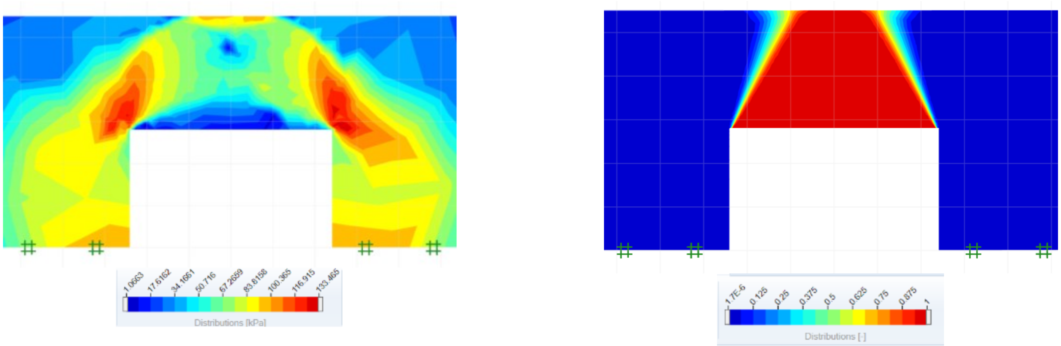

(a) (b)

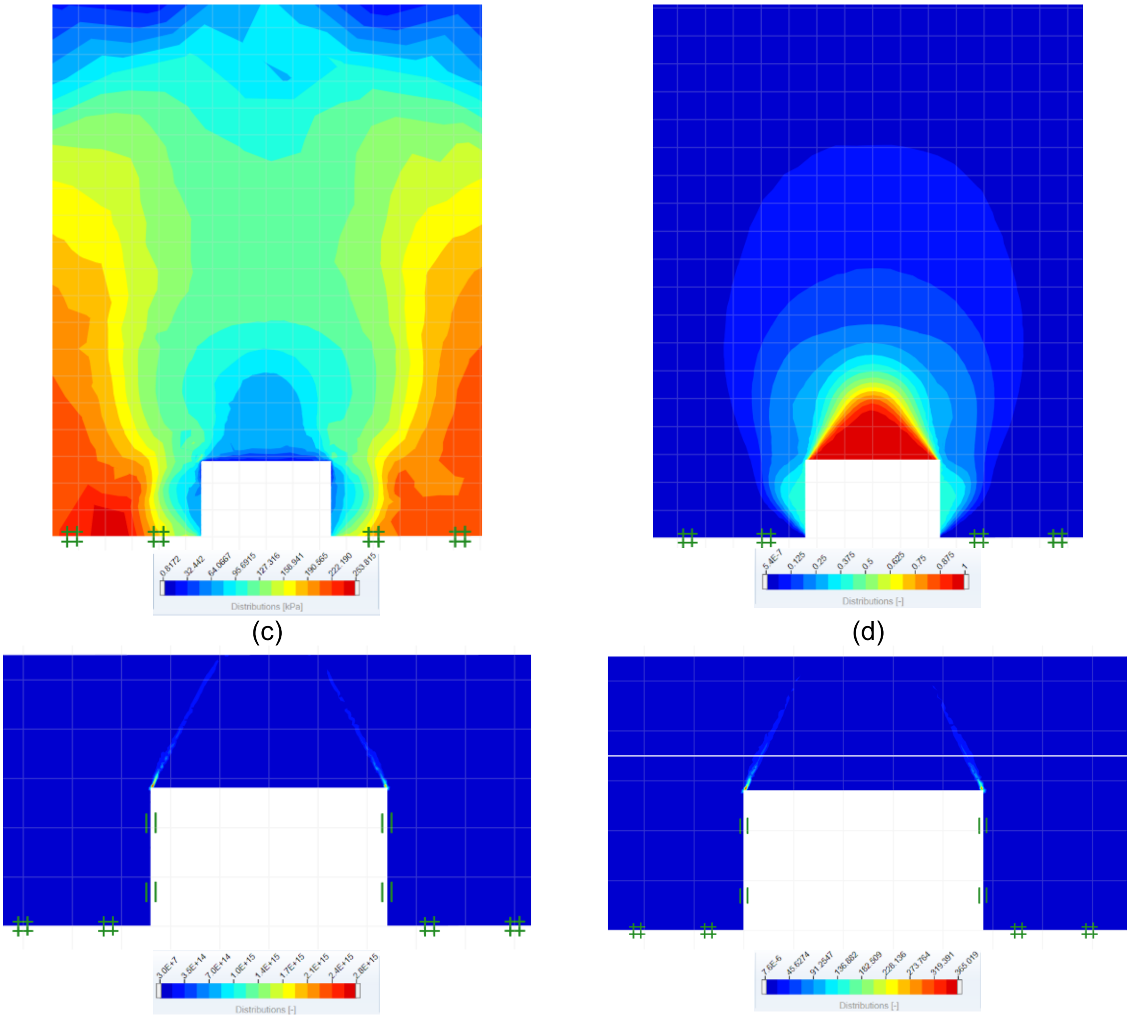

(c) (d)

(e) (f)

Figure 22: (a) Lower bound: deviator stress distribution (kPa). (b) Upper bound: displacement field, |u|. (c) Lower bound for augmented roof thickness: deviator stress distribution (kPa). (d) Upper bound for augmented roof thickness: displacement field, |u|. (e) Elasto-plastic FEM analysis with homogenous stiffness, deviatoric strain, $|\varepsilon_1-\varepsilon_3|$. (f) Elasto-plastic FEM analysis with heterogeneous stiffness, deviatoric strain, $|\varepsilon_1-\varepsilon_3|$